HAL
open science

Neutrophil adhesion in brain capillaries reduces cortical blood flow and impairs memory function in Alzheimer's disease mouse models.

Jean Cruz Hernández, Oliver Bracko, Calvin Kersbergen, Victorine Muse, Mohammad Haft-Javaherian, Maxime Berg, Laibaik Park, Lindsay Vinarcsik, Iryna Ivasyk, Daniel Rivera, et al.

To cite this version:

Jean Cruz Hernández, Oliver Bracko, Calvin Kersbergen, Victorine Muse, Mohammad Haft-Javaherian, et al.. Neutrophil adhesion in brain capillaries reduces cortical blood flow and impairs memory function in Alzheimer's disease mouse models.. Nature Neuroscience, 2019, 22 (3), pp.413-420. 10.1038/s41593-018-0329-4 . hal-02391317

HAL Id: hal-02391317

https://hal.science/hal-02391317v1

Submitted on 21 Dec 2021

HAL is a multi-disciplinary open access archive for the deposit and dissemination of scientific research documents, whether they are published or not. The documents may come from teaching and research institutions in France or abroad, or from public or private research centers.

L'archive ouverte pluridisciplinaire **HAL**, est destinée au dépôt et à la diffusion de documents scientifiques de niveau recherche, publiés ou non, émanant des établissements d'enseignement et de recherche français ou étrangers, des laboratoires publics ou privés.

OATAO
Open Archive Toulouse Archive Ouverte

Open Archive Toulouse Archive Ouverte

OATAO is an open access repository that collects the work of Toulouse researchers and makes it freely available over the web where possible

This is an author's version published in: http://oatao.univ-toulouse.fr/22901

Official URL:

https://doi.org/10.1038/s41593-018-0329-4

To cite this version:

Cruz Hernández, Jean C. and Bracko, Oliver and Kersbergen… [et al.]. Neutrophil adhesion in brain capillaries reduces cortical blood flow and impairs memory function in Alzheimer's disease mouse models. (2019) Nature Neuroscience, 22. 413-420. ISSN 1097-6256

Any correspondence concerning this service should be sent to the repository administrator: tech-oatao@listes-diff.inp-toulouse.fr

Neutrophil adhesion in brain capillaries reduces cortical blood flow and impairs memory function in Alzheimer's disease mouse models

Jean C. Cruz Hernández[1,7], Oliver Bracko[1,7], Calvin J. Kersbergen[1], Victorine Muse[1], Mohammad Haft-Javaherian[1], Maxime Berg[2], Laibaik Park[3], Lindsay K. Vinarcsik[1], Iryna Ivasyk[1], Daniel A. Rivera[1], Yiming Kang[1], Marta Cortes-Canteli[4,5], Myriam Peyrounette[2], Vincent Doyeux[2], Amy Smith[2], Joan Zhou[1], Gabriel Otte[1], Jeffrey D. Beverly[1], Elizabeth Davenport[1], Yohan Davit[2], Charles P. Lin[6], Sidney Strickland[4], Costantino Iadecola[3], Sylvie Lorthois[1,2], Nozomi Nishimura[1,8*] and Chris B. Schaffer[1,8*]

Cerebral blood flow (CBF) reductions in Alzheimer's disease patients and related mouse models have been recognized for decades, but the underlying mechanisms and resulting consequences for Alzheimer's disease pathogenesis remain poorly understood. In APP/PS1 and 5xFAD mice we found that an increased number of cortical capillaries had stalled blood flow as compared to in wild-type animals, largely due to neutrophils that had adhered in capillary segments and blocked blood flow. Administration of antibodies against the neutrophil marker Ly6G reduced the number of stalled capillaries, leading to both an immediate increase in CBF and rapidly improved performance in spatial and working memory tasks. This study identified a previously uncharacterized cellular mechanism that explains the majority of the CBF reduction seen in two mouse models of Alzheimer's disease and demonstrated that improving CBF rapidly enhanced short-term memory function. Restoring cerebral perfusion by preventing neutrophil adhesion may provide a strategy for improving cognition in Alzheimer's disease patients.

Alzheimer's disease is the most common form of dementia in the elderly, worldwide. This disease is characterized by a rapid and progressive cognitive decline accompanied by several pathological features, such as the accumulation of amyloid-beta (Aβ) plaques in brain tissue and along blood vessels as cerebral amyloid angiopathy, the hyperphosphorylation of tau proteins and formation of neurofibrillary tangles in neurons, increased density and activation of inflammatory cells and, ultimately, the death of neurons and other brain cells[1].

Vascular dysfunction is implicated in the pathogenesis of Alzheimer's disease. Many of the primary risk factors are associated with compromised vascular structure and function, such as obesity, diabetes, atherosclerosis and hypertension[2]. Brain blood flow is also severely compromised; cortical cerebral blood flow (cCBF) reductions of ~25% are evident early in disease development in both patients with Alzheimer's disease[3–5] and in mouse models[6–8], which express mutated genes that encode for amyloid precursor protein (APP). Several mechanisms for this hypoperfusion have been proposed, including constriction of brain arterioles[9], loss of vascular density[10] and changes in neural activity patterns and/or in neurovascular coupling[11,12], but a full understanding of the underlying mechanisms for CBF reduction in Alzheimer's disease has not emerged.

These large decreases in blood flow may contribute to the cognitive symptoms of Alzheimer's disease and drive disease progression. Cognitive functions, such as attention, were immediately impaired by a reduction in CBF of ~20% in healthy humans[13]. When CBF was chronically reduced by ~35% in WT mice, spatial memory deficits were observed accompanied by pathological changes in the brain including increased inflammation[14]. In addition, impairing blood flow in Alzheimer's disease mouse models led to an increase in Aβ deposition, suggesting that blood flow deficits can worsen Aβ pathology[14,15]. These data suggest that decreased CBF in Alzheimer's disease probably contributes to both cognitive dysfunction and disease progression.

Because reductions in CBF are a recognized and important aspect of Alzheimer's disease, yet have not been well explained, we sought to uncover the cellular basis for this phenomenon in APP/PS1 and 5xFAD mouse models of APP overexpression.

Results

To investigate cortical hypoperfusion in Alzheimer's disease, we used in vivo two-photon excited fluorescence (2PEF) microscopy to image the cortical vasculature in APP/PS1 mice[16] (Fig. 1a), looking for occluded vessels (Fig. 1b). We observed no obstructions in arterioles or venules, but around 1.8% of capillaries in APP/PS1

[1]Nancy E. and Peter C. Meinig School of Biomedical Engineering, Cornell University, Ithaca, NY, USA. [2]Institut de Mécanique des Fluides de Toulouse, Université de Toulouse, CNRS, INPT, UPS, Toulouse, France. [3]Feil Family Brain and Mind Research Institute, Weill Cornell Medicine, New York, NY, USA. [4]Patricia and John Rosenwald Laboratory for Neurobiology and Genetics, The Rockefeller University, New York, NY, USA. [5]Centro Nacional de Investigaciones Cardiovasculares Carlos III, Madrid, Spain. [6]Wellman Center for Photomedicine and Center for Systems Biology, Massachusetts General Hospital, Harvard Medical School, Boston, MA, USA. [7]These authors contributed equally: Jean C. Cruz Hernández, Oliver Bracko. [8]These authors jointly supervised this work: Nozomi Nishimura, Chris B. Schaffer. *e-mail: nn62@cornell.edu; cs385@cornell.edu

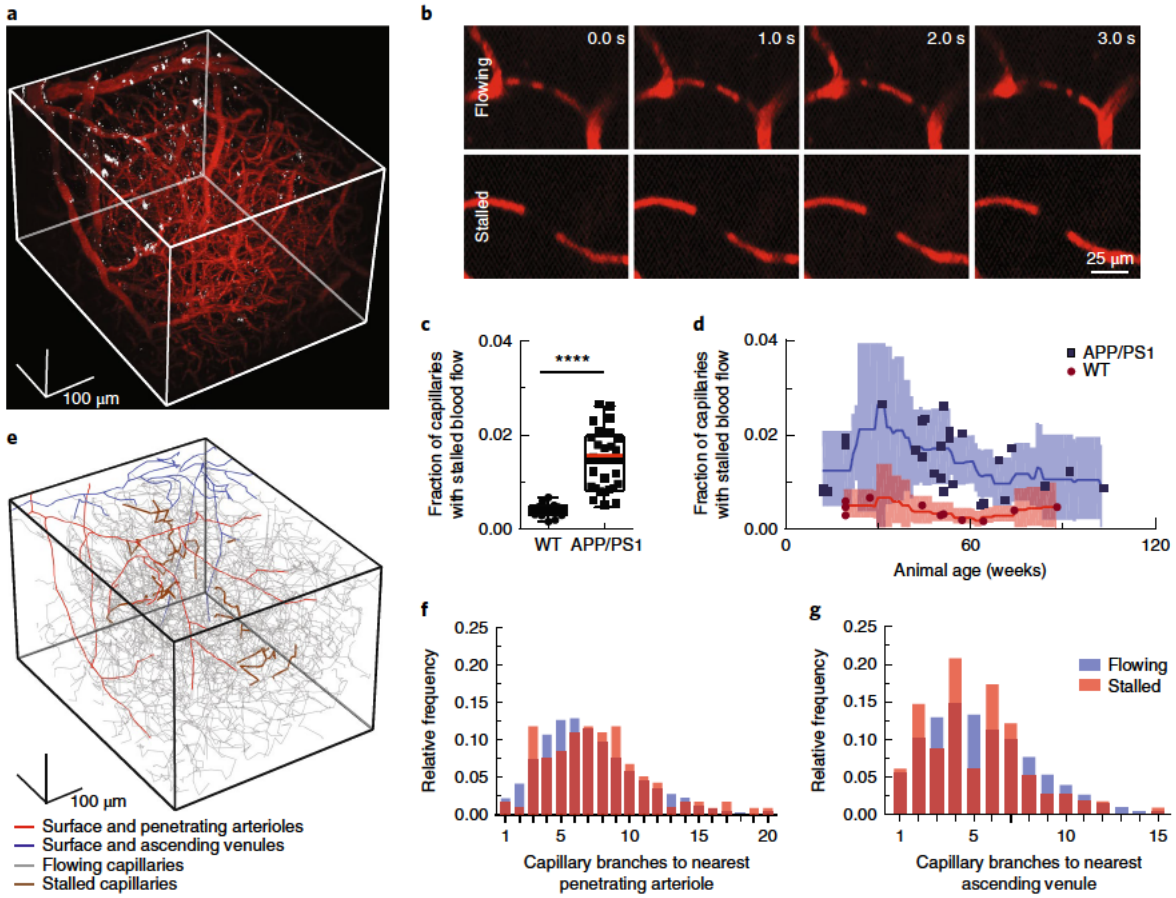

Fig. 1 | 2PEF imaging of mouse cortical vasculature revealed a higher fraction of plugged capillaries in APP/PS1 mice. a, Rendering of 2PEF image stack of cortical vasculature (red; Texas Red dextran) and amyloid deposits (white; methoxy-X04). **b**, Individual brain capillaries were scored as either flowing or stalled based on the motion of unlabeled blood cells (black) within the fluorescently labeled blood plasma (red). **c**, Fraction of capillaries with stalled blood flow in APP/PS1 and WT mice. (APP/PS1: $n = 28$ mice (7 female, 21 male), ~22,400 capillaries, and WT: $n = 12$ mice (10 female, 2 male), ~9,600 capillaries; two-tailed Mann–Whitney test, $P = 6.8 \times 10^{-9}$; boxplot: whiskers extend 1.5 times the difference between the value of the 75th and 25th percentiles, median = black line and mean = red line.) **d**, Same data as in **c**, shown as a function of animal age. Each data point represents the fraction of capillaries stalled in one mouse, with a minimum of 800 capillaries scored per mouse. Curves represent sliding averages with a 10-week window and shaded areas represent 95% confidence intervals. Data from one outlier mouse not shown in **c** and **d**: APP/PS1, 42 weeks, 4.4% stalled. **e**, Tracing of the vascular network in **a**, with stalled capillaries indicated in brown. **f**,**g**, Histograms showing the topological location of flowing and stalled capillaries in APP/PS1 mice relative to the nearest penetrating arteriole and ascending venule, respectively ($n = 8$ mice (5 female, 3 male), 120 stalled and ~8,700 flowing capillaries).

mice had stalled blood flow while age- and sex-matched WT littermates showed absence of flow in 0.4% of capillaries (Fig. 1c; Supplementary Videos 1 and 2). The number of stalled capillaries was elevated by 12 weeks of age in APP/PS1 mice, and remained elevated throughout disease progression (Fig. 1d). Flowing and stalled capillaries (Fig. 1e) showed similar distance distributions relative to the nearest penetrating arteriole (Fig. 1f) or ascending venule (Fig. 1g). The incidence of capillary stalling did not increase with Aβ plaque density (Supplementary Fig. 1a), and was identical in both conscious and anesthetized animals (Supplementary Videos 3 and 4; Supplementary Fig. 1b). Capillary stalling was similarly elevated in 5–6-month-old 5xFAD (Supplementary Fig. 2a) and 10–13-month-old TgCRND8 mice[17] (Supplementary Fig. 3), two different mouse models of APP overexpression.

Using labeling strategies to distinguish leukocytes, platelets, and red blood cells (RBCs) (Fig. 2a), we found that the majority of stalled capillary segments in APP/PS1 mice contained a leukocyte, sometimes with and sometimes without one or more RBCs also present in the capillary segment (Fig. 2b). We injected a low dose of fluorescently labeled antibodies against Ly6G, a neutrophil surface marker (0.1 mg kg^{-1} animal weight, intravenous), and found that the vast majority of capillary stalls had a labeled cell present (Fig. 2c; 26 of 30 identified capillary stalls across four mice were labeled). Stalled capillaries had a modestly lower average diameter than flowing capillaries (Fig. 2d), but no difference in the density of nearby Aβ deposits (Fig. 2e). Most plugged capillaries were transiently stalled with a half-life of <5 min, while one-third remained stalled for 15 min and 10% began flowing and then re-stalled within 15 min (Fig. 2f; Supplementary Fig. 4). We also observed that some capillary segments alternated between flowing and stalled in repeated imaging sessions over weeks (Fig. 2g). The same capillaries were stalled across multiple imaging sessions about ten times as frequently as predicted by a statistical model that assumed each capillary had an equal probability of being stalled at any time point (Fig. 2h). Taken together, these data suggest that the capillary stalls were caused by leukocytes (probably neutrophils based on the specificity of Ly6G expression[18]) plugging a distinct subset of capillary segments.

We serendipitously found that administration of a much higher dose of fluorescently labeled antibodies against Ly6G (α-Ly6G; 4 mg kg^{-1} animal weight, intraperitoneal) reduced the number of stalled capillaries within 10 min (Fig. 3a; Supplementary Fig. 5). Isotype control (Iso-Ctr) antibodies did not impact capillary stalling.

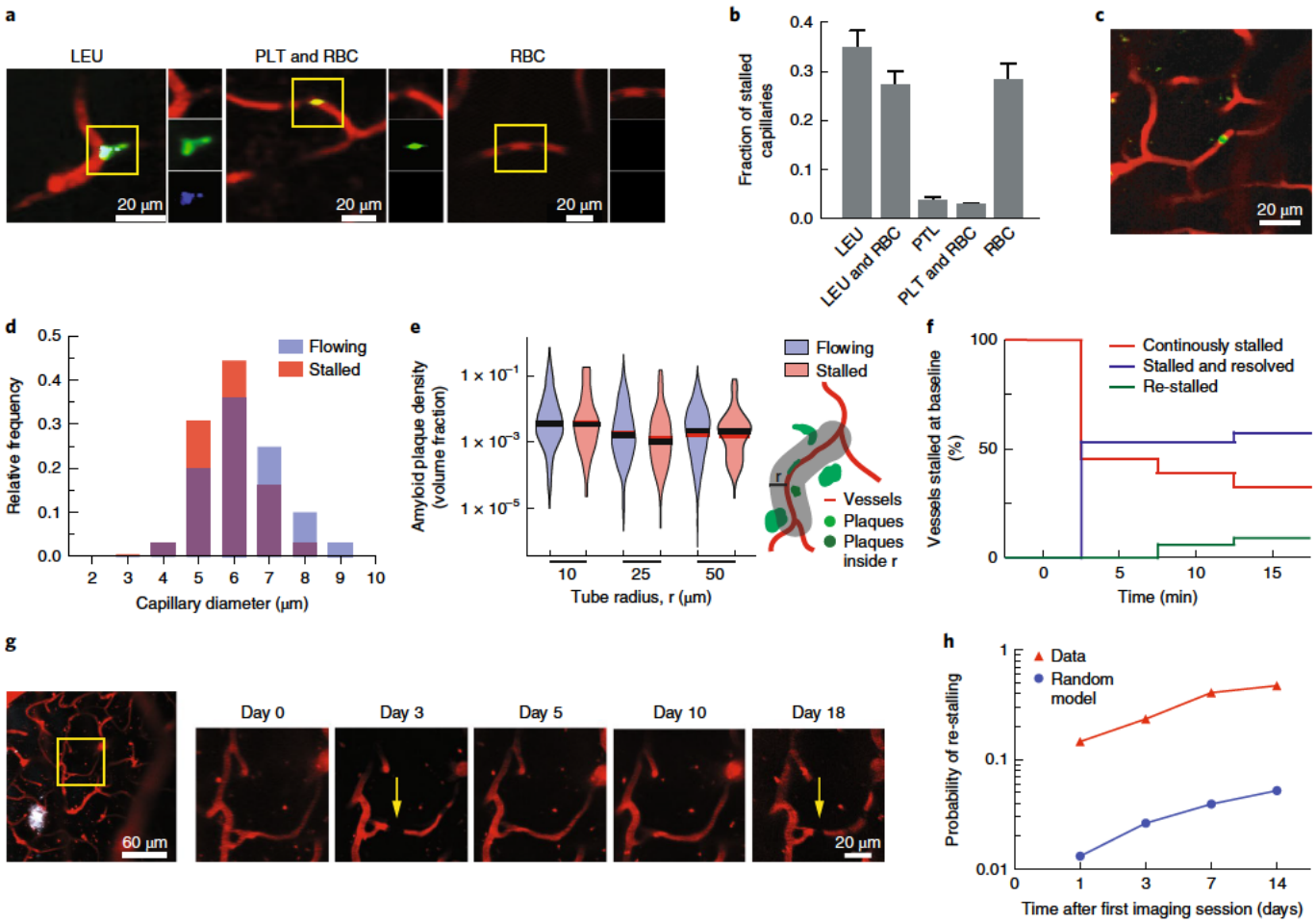

Fig. 2 | Characterization of the cause, location and dynamics of capillary occlusions in APP/PS1 mice. a, 2PEF images of stalled capillaries that contained a leukocyte (LEU, left), platelet aggregates (PLT) and RBCs (center), or only RBCs (right), distinguished by fluorescent labels (red, Texas Red-labeled blood plasma; green, rhodamine 6G-labeled leukocytes and platelets; blue, Hoechst-labeled leukocyte nuclei). **b**, Fraction of stalled capillaries in APP/PS1 mice that contained LEU, one or more RBCs and PLT, distinguishing cases of LEU only, LEU with one or more RBCs, PLT only, PLT with RBCs, and RBCs only ($n = 6$ mice (3 female, 3 male) and 106 stalls; error bars represent 95% confidence intervals based on binomial statistics.) **c**, Projection of 2PEF image stack showing an anti-Ly6G-labeled cell in a stalled capillary (red, Texas Red-labeled blood plasma; green, anti-Ly6G-Alexa488 (0.1 mg kg^{-1} animal weight, intravenous). **d**, Histogram of the diameter of flowing and stalled capillaries in APP/PS1 mice (averages: 5.8 ± 0.84 μm (stalled), 6.3 ± 1.1 μm (flowing) (mean ± s.d.); two-tailed Mann–Whitney test, $P = 0.000020$; $n = 7$ mice (4 female, 3 male), 116 stalled and ~8,400 flowing capillaries). **e**, Violin plot of the density of amyloid deposits within tubes of different radius that followed the capillary centerline for flowing and stalled capillary segments in APP/PS1 mice ($n = 7$ mice (4 female, 3 male), 116 stalled and ~8,400 flowing capillaries). The vertical range of the violin plot represents the full range of measured values, while the width indicates the frequency of those values. The red (or black) horizontal line indicates the mean (or median) value. **f**, Fraction of stalled capillaries that remained stalled (red), resumed flowing (green) or resumed flowing and then re-stalled (blue) over 15 min in APP/PS1 mice ($n = 3$ mice (all male), 31 capillary segments). **g**, 2PEF images of the same capillary alternately stalled (arrows) and flowing over several weeks (white, methoxy-X04). **h**, Probability of an initially stalled capillary observed as stalled again at any subsequent imaging time point, showing both real observations in APP/PS1 mice and predictions from a model that assumed each capillary had an equal probability of stalling at each time point ($n = 4$ mice (2 female, 2 male), 49 stalled capillaries followed from the first imaging session).

Using flow cytometry (Supplementary Fig. 6a), we found that α-Ly6G administration led to no change in the number of circulating neutrophils at 3 h (Supplementary Fig. 6b), but did lead to ~50% depletion by 6 h (Supplementary Fig. 6c) and near complete depletion by 24 h (Supplementary Fig. 6d). Median volumetric blood flow in penetrating arterioles, measured using 2PEF (Fig. 3b) and characterizing blood flow into the cortex, increased by 26% in young (3–4 months) and by 32% in aged (11–14 months) APP/PS1 mice 1 h after α-Ly6G administration (Fig. 3c). This increase in penetrating arteriole blood flow was due to an increase in RBC velocity rather than to an increase in vessel diameter (Supplementary Fig. 7a,b). Penetrating arterioles with lower baseline flow tended to show higher flow increases (Supplementary Fig. 7c). Iso-Ctr antibodies did not change penetrating arteriole blood flow in APP/PS1 mice, nor did α-Ly6G in WT animals (Fig. 3c). We also used arterial spin-labeled magnetic resonance imaging (ASL-MRI) to measure cCBF in 7–9-month-old animals (Fig. 3d). At baseline, average cCBF in APP/PS1 mice was 17% lower than in WT animals (Fig. 3e). We observed an increase in cCBF of 13% in APP/PS1 mice at ~5 h after α-Ly6G administration, recovering about two-thirds of the deficit relative to WT animals, but this was unchanged in APP/PS1 mice administered Iso-Ctr antibodies or WT mice given α-Ly6G (Fig. 3e). To establish the timeline for these CBF increases, we used multi-exposure laser speckle contrast imaging to quantify changes in CBF over the first 3 h after antibody administration in APP/PS1 mice. CBF increased within the first 10 min after α-Ly6G

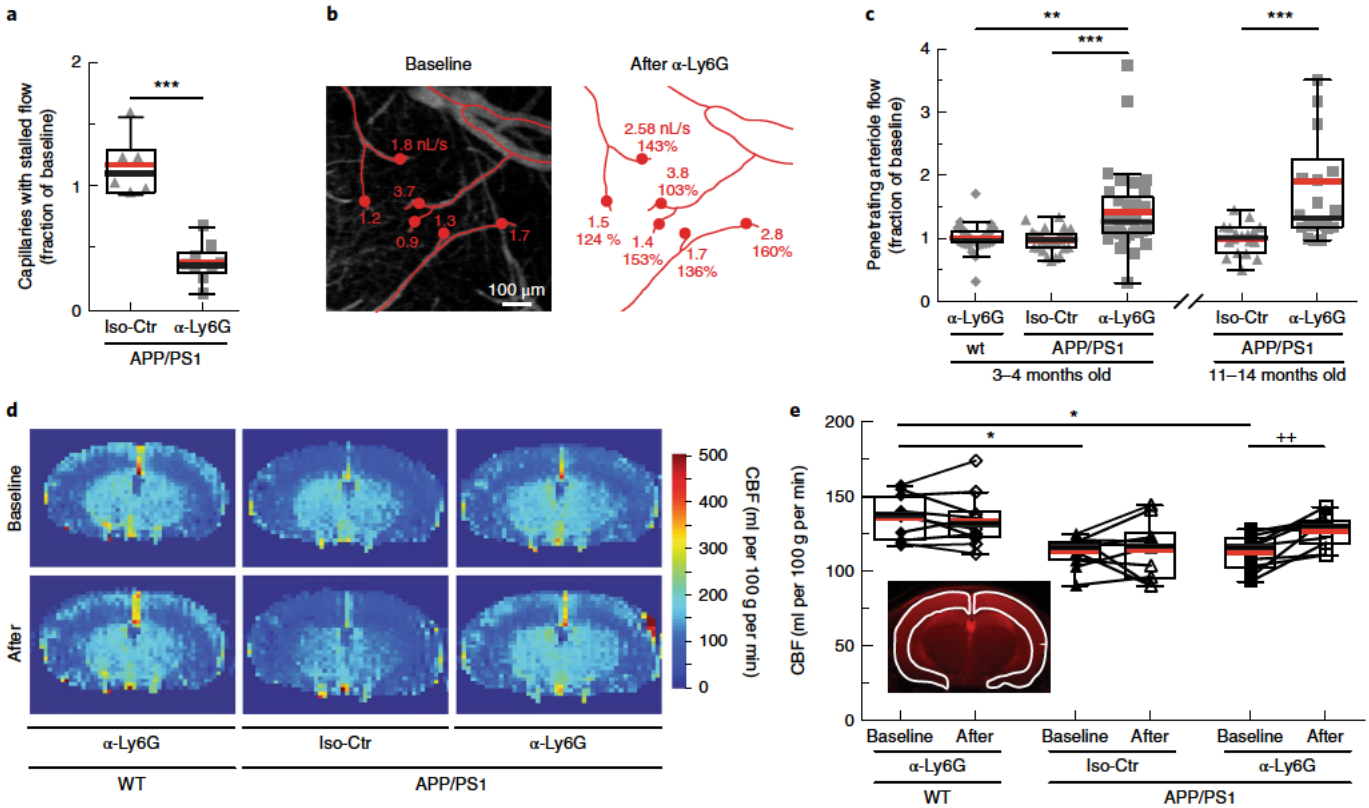

Fig. 3 | Administration of antibodies against Ly6G reduced the number of stalled capillaries and increased cCBF in APP/PS1 mice. a, Number of capillaries with stalled blood flow ~1 h after α-Ly6G or Iso-Ctr antibody administration (4 mg kg^{-1} animal weight, intraperitoneal) shown as a fraction of the number of stalled capillaries at baseline in APP/PS1 mice (α-Ly6G: $n=6$ mice (3 female, 3 male), ~4,800 capillaries; Iso-Ctr: $n=6$ mice (5 female, 1 male), ~4,800 capillaries; two-tailed Mann–Whitney test, $P=0.0004$). **b**, Projection of 2PEF image stack of brain surface vasculature, with surface (red lines) and penetrating (red dots) arterioles identified. For each penetrating arteriole, volumetric blood flow is indicated at baseline (left) and after α-Ly6G administration (right), along with the percentage of baseline flow. **c**, Volumetric blood flow in penetrating arterioles measured 60–90 min after α-Ly6G or Iso-Ctr antibody administration in young and old APP/PS1 mice and WT control animals, shown as a fraction of baseline arteriole flow (young APP/PS1 Iso-Ctr: $n=5$ mice (1 female, 4 male), 32 arterioles; old APP/PS1 Iso-Ctr: $n=3$ mice (1 female, 2 male), 18 arterioles; young WT α-Ly6G: $n=5$ mice (3 female, 2 male), 30 arterioles; young APP/PS1 α-Ly6G: $n=5$ (2 female, 3 male), 33 arterioles; old APP/PS1 α-Ly6G: $n=3$ mice (all male), 22 arterioles; one-way Kruskal–Wallis ANOVA with post hoc Dunn's multiple-comparison correction: young WT α-Ly6G versus young APP/PS1 α-Ly6G $P=0.0023$; young APP/PS1 Iso-Ctr versus young APP/PS1 α-Ly6G $P=0.0000012$; old APP/PS1 Iso-Ctr versus old APP/PS1 α-Ly6G $P=0.00055$). **d**, CBF map measured using ASL-MRI at baseline and ~5 h after administration of α-Ly6G or Iso-Ctr antibodies in APP/PS1 and WT mice. **e**, cCBF measurements (ASL-MRI, inset indicates region of interst on T2 MRI image) at baseline and ~5 h after administration of α-Ly6G or Iso-Ctr antibodies in APP/PS1 and WT mice (WT α-Ly6G: $n=10$ mice, APP/PS1 α-Ly6G: $n=10$ mice, APP/PS1 Iso-Ctr: $n=10$ mice; ordinary ANOVA with post hoc Tukey's multiple-comparison correction to compare across groups: baseline WT α-Ly6G versus baseline APP/PS1 α-Ly6G $P=0.011$; baseline WT α-Ly6G versus baseline APP/PS1 Iso-Ctr $P=0.014$; paired t test to compare baseline and after treatment within a group: baseline APP/PS1 α-Ly6G versus after APP/PS1 α-Ly6G $P=0.0058$). All boxplots: whiskers extend 1.5 times the difference between the value of the 75th and 25th percentiles; median, black line; mean, red line.

administration and remained elevated over 3 h (Supplementary Fig. 8). Isotype control antibodies did not lead to major changes in CBF (Supplementary Fig. 8). In 5–6-month-old 5xFAD mice; we also found that α-Ly6G administration led to both a reduction in the number of stalled capillaries (Supplementary Fig. 2a) and an increase in blood flow in cortical penetrating arterioles (Supplementary Fig. 2b–d) within 1 h. Thus, administration of α-Ly6G led to a rapid reduction in the number of capillary stalls that was accompanied by a rapid increase in cCBF in APP/PS1 and 5xFAD mice. In contrast, when antibodies against LFA-1 were administered to 11–13-month-old APP/PS1 mice, we did not observe a rapid decrease in the number of stalled capillaries. Instead, we found that capillary stalls were reduced and penetrating arteriole blood flow was increased 1 day after antibody injection, when circulating leukocytes had been depleted (Supplementary Fig. 9). Across all antibody and control treatments in APP/PS1 mice, penetrating arteriole flows increased (decreased) when the number of stalled capillaries decreased (increased) (Supplementary Fig. 9g).

We next tested whether administration of α-Ly6G would improve cognitive function in APP/PS1 (Fig. 4a) and 5xFAD mice. In the object replacement test of spatial short-term memory (Fig. 4b), a single dose of α-Ly6G in ~11-month-old APP/PS1 mice improved performance to the level of WT animals at 3 and 24 h after administration (Fig. 4c; Supplementary Fig. 10a). APP/PS1 mice treated with Iso-Ctr antibodies showed no change, nor did WT animals administered α-Ly6G (Fig. 4c). In ~6-month-old 5xFAD mice, a single dose of α-Ly6G improved performance in the object replacement task at 24 h, with this trend evident at 3 h (Supplementary Fig. 11a,b). Similarly, α-Ly6G improved the performance of APP/PS1 and 5xFAD mice in the Y-maze test of working memory (Fig. 4d; Supplementary Figs. 10b, 11c,d). We detected no improvement in sensory motor function (balance beam walk, Supplementary Fig. 12a–d) nor in depression- and anxiety-like behavior (forced swim, Supplementary Fig. 12e) in APP/PS1 mice administered α-Ly6G. To exclude an antibody-specific effect, we repeated the object replacement and Y-maze behavioral tests in another cohort

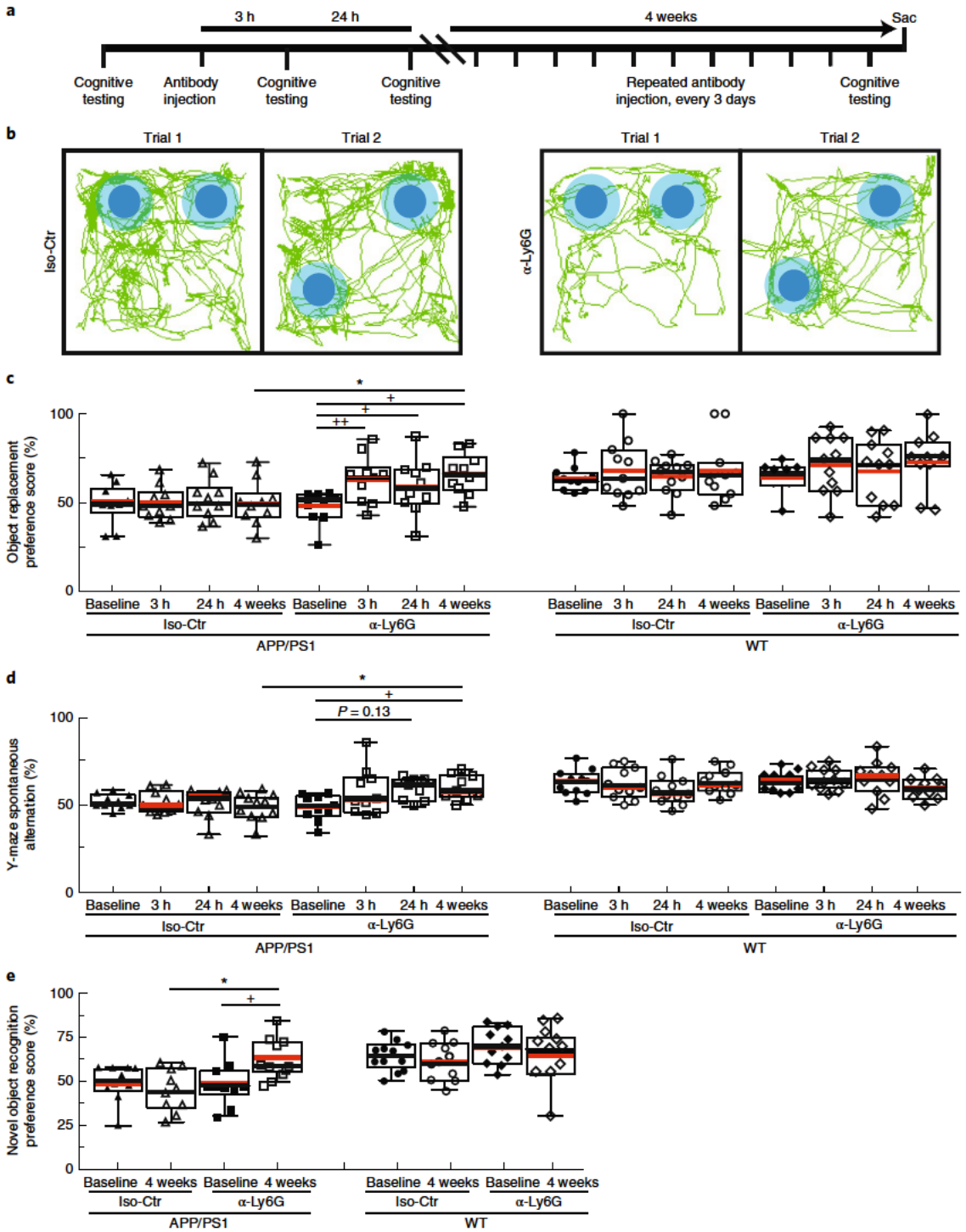

Fig. 4 | Administration of α-Ly6G improved short-term memory. a, Experimental timeline for behavioral studies. Sac, date the animal was killed for analysis. **b**, Tracking of mouse nose location from video recording during training and trial phases of object replacement task taken 3–5 h after administration of α-Ly6G or Iso-Ctr antibodies in APP/PS1 mice (representative tracing maps). **c**,**d**, Preference score in object replacement task (**c**) and spontaneous alternation in Y-maze task (**d**) for APP/PS1 and WT mice at baseline and at 3 h and 24 h after a single administration of α-Ly6G or Iso-Ctr antibody and after 4 weeks of treatment every 3 days. **e**, Preference score in the NOR task for APP/PS1 and WT mice at baseline and after 4 weeks of treatment every 3 days. (APP/PS1 Iso-Ctr: $n=10$ mice (5 female, 5 female), APP/PS1 α-Ly6G: $n=10$ mice (5 female, 5 male), WT α-Ly6G: $n=11$ mice (7 female, 4 male), WT Iso-Ctr: $n=11$ mice (8 female, 3 male); one-way Kruskal–Wallis ANOVA with post hoc Dunn's multiple-comparison correction to compare across groups: object replacement APP/PS1 4 weeks Iso-Ctr versus α-Ly6G $P=0.029$; Y-maze APP/PS1 4 weeks Iso-Ctr versus α-Ly6G $p=0.037$; novel object APP/PS1 4 weeks Iso-Ctr versus α-Ly6G $P=0.038$; Friedman one-way repeated measures non-parametric ANOVA to compare baseline and after-treatment results within a group: object replacement APP/PS1 α-Ly6G baseline versus 3 h $P=0.0055$, baseline versus 24 h $P=0.016$, baseline versus 4 weeks $P=0.045$; Y-maze APP/PS1 α-Ly6G baseline versus 24 h $P=0.13$, baseline versus 4 weeks $P=0.036$; two-tailed Wilcoxon matched-pairs signed-rank test to compare baseline and post-treatment with novel object APP/PS1 α-Ly6G baseline versus 4 weeks $P=0.039$.) All boxplots: whiskers extend 1.5 times the difference between the value of the 75th and 25th percentiles; median, black line; mean, red line. All data in this figure represent the aggregation of two independently conducted sets of behavioral experiments.

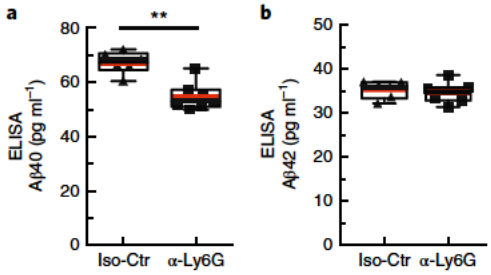

Fig. 5 | Administration of α-Ly6G for one month decreased the concentration of $A\beta_{1-40}$ in APP/PS1 mice. a,b, Enzyme-linked immunosorbent assay (ELISA) measurements of (**a**) Aβ1–40 and (**b**) Aβ1–42 monomer concentrations after 4 weeks of treatment every 3 days (Iso-Ctr: $n = 6$ mice (4 female, 2 male) and α-Ly6G: $n = 7$ mice (4 female, 3 male); two-tailed Mann–Whitney test, $P = 0.0023$). Boxplots: whiskers extend 1.5 times the difference between the value of the 75th and 25th percentiles; median, black line; mean, red line.

of APP/PS1 mice before and after administration of α-LFA-1 antibodies, and found improved performance in both tests at 24 h (Supplementary Fig. 13a–d).

We continued to treat the APP/PS1 mice that received α-Ly6G with additional doses of α-Ly6G every 3 days for one month, resulting in depletion of neutrophils (Supplementary Fig. 6e). After this regimen, APP/PS1 mice exhibited short-term memory performance that matched WT animals in object replacement (Fig. 4c), Y-maze (Fig. 4d) and novel object recognition (NOR) (Fig. 4e; Supplementary Fig. 10c,d). We saw no improvement in sensory motor function (Supplementary Fig. 12a–d) nor in depression- and anxiety-like behavior (Supplementary Fig. 12e).

Because one of the clearance pathways for Aβ is through the vasculature[19], we assessed whether improving cCBF with α-Ly6G would reduce the concentration of Aβ monomers and aggregates. Using enzyme-linked immunosorbent assay of brain extracts from the animals that received antibody treatment for one month, we found that α-Ly6G reduced the concentration of $A\beta_{1-40}$ compared to Iso-Ctr antibodies (Fig. 5a), while the concentration of $A\beta_{1-42}$ (Fig. 5b) and aggregates of Aβ (Supplementary Fig. 14d) remained unchanged. We saw no difference in the number and density of Aβ plaques between α-Ly6G- and Iso-Ctr-treated animals (Supplementary Fig. 14a–c).

Finally, we addressed the question of how only ~2% of capillaries being stalled could explain the dramatic blood flow changes we observed after administration of α-Ly6G. Because each occluded capillary decreases blood flow in both up- and downstream vessels[20], a small number of stalled capillaries could have an outsized impact on CBF. To estimate the magnitude of this impact and to compare how the topology of the cortical capillary network influences the result, we simulated blood flow in vascular networks from a 1 mm^3 volume of mouse parietal cortex (Fig. 6a)[21], a 6 mm^3 volume of human cortex (Fig. 6b)[22] and a synthetic periodic network of order three (Supplementary Fig. 15a) using a nonlinear model of microvascular blood flow[23] (see Supplementary Methods and Supplementary Note). cCBF decreased linearly with an increasing fraction of stalled capillaries, without any threshold effect, across all three networks (Fig. 6c) demonstrating that, on average, each single capillary occlusion has a similar, and cumulative, impact on blood flow. Moreover, the slope of the CBF decrease with increasing capillary stalls was almost identical among the mouse, human and artificial networks, suggesting that capillary stalling may impact CBF similarly across three-dimensional capillary networks with three vessels connected at each node. Quantitatively, these simulations predicted a ~5% (10%) deficit in cCBF due to 2% (4%) of capillaries being stalled (relative to the case with no capillary stalls), which is less than the increase in CBF we observed with 2PEF and ASL-MRI measurements after administration of α-Ly6G.

Discussion

In this study, we aimed to uncover the cellular mechanisms contributing to reduced cCBF in Alzheimer's disease and to determine the impact of this reduction on cognitive function. Brain blood flow reductions occur in the vast majority of dementia patients, including those with Alzheimer's disease. This phenomenon is amomg the earliest features of Alzheimer's disease progression[3,24]. Mouse models that express mutant APP also show comparable reductions in CBF[6–8].

Previous studies have implicated a variety of potential mechanisms involved in the reduced CBF seen in Alzheimer's disease. Amyloid-beta monomers were found to drive vasoconstriction in brain arterioles, potentially contributing to a reduction in resting CBF[9]. In Alzheimer's disease there is a more rapid loss of vascular density with age, which could reduce cerebral perfusion[10]. In addition to reduction in baseline perfusion, regulation of blood flow in the brain is compromised in Alzheimer's disease. Vessel diameter changes in response to CO_2 inhalation and changes in both blood pressure and local neural activity were attenuated in both Alzheimer's patients and mouse models of APP overexpression[25]. This loss of dynamic regulation of CBF could also contribute to cognitive impacts. Indeed, recent work showed that restoring cerebrovascular function, by either angiotensin receptor inhibition or reduction of vascular oxidative stress, led to improved cognitive function[12,26,27].

Our data reveal that neutrophil plugging of individual capillary segments is a previously unrecognized mechanism that contributes largely to reduced CBF in Alzheimer's disease mouse models. The rapid resolution of capillary stalls after α-Ly6G treatment suggests that they are caused by receptor-mediated interactions of neutrophils with the capillary endothelium[28], probably due to increased endothelial inflammation. Ly6G has long been recognized as a neutrophil-specific marker[29]. Consistent with our findings, it has recently been shown that inhibition of Ly6G signaling leads to decreased migration of neutrophils toward sites of inflammation by modulation of β2-integrin-dependent adhesion[28]. There may, however, be other mechanisms that contribute to the reduction in capillary stalling after α-Ly6G treatment. We observed that stalled capillaries had a moderately smaller diameter, on average, than flowing capillaries, and a receptor-mediated increase in the mechanical stiffness of neutrophils that was blocked by α-Ly6G might allow for easier deformation and passage of neutrophils through narrowed capillaries[30]. While certain mouse models of Alzheimer's disease have shown marked alteration in the topology of the cortical vascular network, recent work has shown that there are relatively minor differences in the capillary density and tortuosity between APP/PS1 and WT mice, suggesting that differences in vascular structure probably do not underlie any increase in capillary stalling in APP/PS1 mice[31,32].

Capillary obstruction due to tissue inflammation has been observed in a variety of organ systems (typically at higher incidence than observed here), and has been shown to contribute to the development of pathology and disease[33–39]. Inflammation is a persistent and well-recognized feature of Alzheimer's disease, and previous work has demonstrated an increase in inflammatory adhesion receptors on endothelial cells[40–42], which probably underlies the capillary stalling we observed. A major contributor to this inflammation is increased reactive oxygen species induced by brain exposure to Aβ oligomeric aggregates[26]. These reactive oxygen species cause a loss of cerebrovascular flow regulation and probably drive the expression of leukocyte-binding receptors on the endothelial

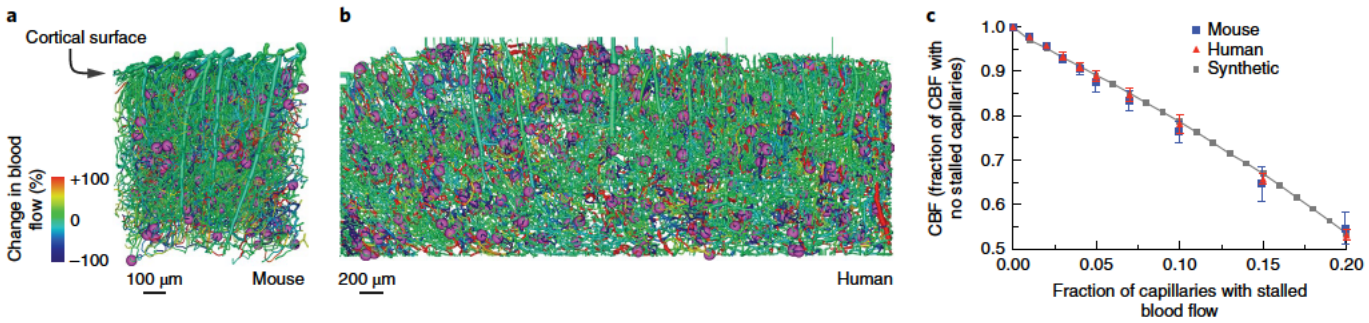

Fig. 6 | Simulations predicted a similar CBF decrease in mouse and human cortical capillary networks with increasing fraction of capillaries with stalled flow. a,b, Spatial maps of simulated blood flow changes caused by stalling of 2% of capillaries (indicated by purple spheres) in a mouse cortical vascular network (**a**) and a human network (**b**). Data on the structure and connectivity of the former (mouse) are derived from ref. [44], and of the latter (human) from ref. [22]. **c**, Normalized cortical perfusion as a function of the fraction of capillaries that were occluded, expressed as a fraction of the perfusion with no occlusions, in mouse, human and synthetic networks (data points represent the mean and error bars represent s.d. across five independent simulations).

cell surface, such as ICAM1 and VCAM1. Our observation that certain capillary segments were more likely to stall suggests that the underlying vascular inflammation may not be uniform.

While our focus in this study has been on increased leukocyte adherence causing the transient stalling of capillaries due to firmly adherent leukocytes, this increased adherence probably also contributes to slowed, but not stalled, flow in other capillary segments when leukocytes are present. Our experimental approach did not enable us to readily detect such slowed vessels; our simulations included only the impact of completely stalled vessels, which may have contributed to the model's underestimation of the increase in CBF after α-Ly6G administration. However, the simulations predicted a similar sensitivity of brain blood flow to capillary stalling in humans and mice, suggesting that, if capillary stalling occurs in Alzheimer's patients, major improvement in blood flow could be achieved.

We observed spatial and working memory improvements within 24 h of treatment with antibodies against Ly6G and LFA-1 in multiple mouse models of Alzheimer's disease. The temporal correlation between reduced capillary stalling/blood flow increase and the improvement in cognitive function suggests that a mismatch between neuronal energy metabolism and delivery of energy substrates through blood flow contributes to the cognitive deficit in these mouse models.

We also observed improved cognitive function after one month of treatment with α-Ly6G, which depletes neutrophils, in APP/PS1 mice, measured during antibody therapy. Because of the persistent depletion of neutrophils during this treatment, we expect that capillary stalling was reduced and brain blood flow increased throughout the month, including during cognitive testing, which probably contributed to the improved cognitive performance. In previous work by Zenaro et al. treatment with antibodies that deplete neutrophils (α-GR-1, α-LFA-1 and α-Ly6G) for one month in multiple Alzheimer's disease mouse models (3xTg and 5xFAD) led remarkably to a persistent improvement in cognitive performance measured one month after the end of antibody therapy[42]. This improvement was attributed to a decrease in the number of neutrophils present in the brain parenchyma, due to antibody-mediated depletion and a resulting decrease in neuro-inflammation, and it is likely that this mechanism contributed to the improvement in cognitive performance we observed after one month of antibody therapy. Taken together, these studies show that neutrophil interactions in the vasculature and parenchyma of the brain play a crucial role in the impaired cognitive function observed in multiple mouse models of amyloid-beta overexpression.

Without a firm understanding of the underlying mechanisms that result in reduced CBF in Alzheimer's disease, no medical approach to increasing brain blood flow has been developed or tested in humans. In a limited series of experiments in severe Alzheimer's patients, a piece of omentum, which is known to secrete angiogenic factors and encourage new vessel growth, was surgically placed on the surface of the brain. In patients showing increased CBF as a result, there were signs of improved cognitive function[5,43]. Accordingly, improving CBF by interfering with neutrophil adhesion could be a promising therapeutic approach in Alzheimer's disease.

Online content

Any methods, additional references, Nature Research reporting summaries, source data, statements of data availability and associated accession codes are available at https://doi.org/10.1038/s41593-018-0329-4.

References

1. Wang, J., Gu, B. J., Masters, C. L. & Wang, Y. J. A systemic view of Alzheimer disease - insights from amyloid-β metabolism beyond the brain. *Nat. Rev. Neurol.* **13**, 612–623 (2017).
2. Santos, C. Y. et al. Pathophysiologic relationship between Alzheimer's disease, cerebrovascular disease, and cardiovascular risk: a review and synthesis. *Alzheimers Dement.* **7**, 69–87 (2017).
3. Iturria-Medina, Y., Sotero, R. C., Toussaint, P. J., Mateos-Pérez, J. M. & Evans, A. C. Early role of vascular dysregulation on late-onset Alzheimer's disease based on multifactorial data-driven analysis. *Nat. Commun.* **7**, 11934 (2016).
4. Dai, W. et al. Mild cognitive impairment and Alzheimer disease: patterns of altered cerebral blood flow at MR imaging. *Radiology* **250**, 856–866 (2009).
5. Wolters, F. J. et al. Cerebral perfusion and the risk of dementia: a population-based study. *Circulation* **136**, 719–728 (2017).
6. Wiesmann, M. et al. Hypertension, cerebrovascular impairment, and cognitive decline in aged AβPP/PS1 mice. *Theranostics* **7**, 1277–1289 (2017).
7. Li, H. et al. Vascular and parenchymal amyloid pathology in an Alzheimer disease knock-in mouse model: interplay with cerebral blood flow. *Mol. Neurodegener.* **9**, 28 (2014).
8. Niwa, K., Kazama, K., Younkin, S. G., Carlson, G. A. & Iadecola, C. Alterations in cerebral blood flow and glucose utilization in mice overexpressing the amyloid precursor protein. *Neurobiol. Dis.* **9**, 61–68 (2002).
9. Niwa, K. et al. A beta-peptides enhance vasoconstriction in cerebral circulation. *Am. J. Physiol. Heart Circ. Physiol.* **281**, H2417–H2424 (2001).
10. Farkas, E. & Luiten, P. G. Cerebral microvascular pathology in aging and Alzheimer's disease. *Prog. Neurobiol.* **64**, 575–611 (2001).
11. Chen, Y. et al. Voxel-level comparison of arterial spin-labeled perfusion MRI and FDG-PET in Alzheimer disease. *Neurology* **77**, 1977–1985 (2011).
12. Royea, J., Zhang, L., Tong, X. K. & Hamel, E. Angiotensin IV receptors mediate the cognitive and cerebrovascular benefits of losartan in a mouse model of Alzheimer's disease. *J. Neurosci.* **37**, 5562–5573 (2017).
13. Marshall, R. S. et al. Recovery of brain function during induced cerebral hypoperfusion. *Brain* **124**, 1208–1217 (2001).

14. Wang, L. et al. Chronic cerebral hypoperfusion induces memory deficits and facilitates Aβ generation in C57BL/6J mice. *Exp. Neurol.* **283**(Pt A), 353–364 (2016).
15. Hattori, Y. et al. Gradual carotid artery stenosis in mice closely replicates hypoperfusive vascular dementia in humans. *J. Am. Heart Assoc.* **5**, e002757 (2016).
16. Radde, R. et al. Abeta42-driven cerebral amyloidosis in transgenic mice reveals early and robust pathology. *EMBO Rep.* **7**, 940–946 (2006).
17. Chishti, M. A. et al. Early-onset amyloid deposition and cognitive deficits in transgenic mice expressing a double mutant form of amyloid precursor protein 695. *J. Biol. Chem.* **276**, 21562–21570 (2001).
18. Hasenberg, A. et al. Catchup: a mouse model for imaging-based tracking and modulation of neutrophil granulocytes. *Nat. Methods* **12**, 445–452 (2015).
19. Deane, R., Bell, R. D., Sagare, A. & Zlokovic, B. V. Clearance of amyloid-beta peptide across the blood-brain barrier: implication for therapies in Alzheimer's disease. *CNS Neurol. Disord. Drug Targets* **8**, 16–30 (2009).
20. Nishimura, N. et al. Targeted insult to subsurface cortical blood vessels using ultrashort laser pulses: three models of stroke. *Nat. Methods* **3**, 99–108 (2006).
21. Tsai, P. S. et al. Correlations of neuronal and microvascular densities in murine cortex revealed by direct counting and colocalization of nuclei and vessels. *J. Neurosci.* **29**, 14553–14570 (2009).
22. Lauwers, F., Cassot, F., Lauwers-Cances, V., Puwanarajah, P. & Duvernoy, H. Morphometry of the human cerebral cortex microcirculation: general characteristics and space-related profiles. *Neuroimage* **39**, 936–948 (2008).
23. Lorthois, S., Cassot, F. & Lauwers, F. Simulation study of brain blood flow regulation by intra-cortical arterioles in an anatomically accurate large human vascular network. Part II: flow variations induced by global or localized modifications of arteriolar diameters. *Neuroimage* **54**, 2840–2853 (2011).
24. Roher, A. E. et al. Cerebral blood flow in Alzheimer's disease. *Vasc. Health Risk Manag.* **8**, 599–611 (2012).
25. Iadecola, C. The neurovascular unit coming of age: a journey through neurovascular coupling in health and disease. *Neuron* **96**, 17–42 (2017).
26. Park, L. et al. Nox2-derived radicals contribute to neurovascular and behavioral dysfunction in mice overexpressing the amyloid precursor protein. *Proc. Natl Acad. Sci. USA* **105**, 1347–1352 (2008).
27. Park, L. et al. Innate immunity receptor CD36 promotes cerebral amyloid angiopathy. *Proc. Natl Acad. Sci. USA* **110**, 3089–3094 (2013).
28. Wang, J. X. et al. Ly6G ligation blocks recruitment of neutrophils via a β 2-integrin-dependent mechanism. *Blood* **120**, 1489–1498 (2012).
29. Daley, J. M., Thomay, A. A., Connolly, M. D., Reichner, J. S. & Albina, J. E. Use of Ly6G-specific monoclonal antibody to deplete neutrophils in mice. *J. Leukoc. Biol.* **83**, 64–70 (2008).
30. Lavkan, A. H., Astiz, M. E. & Rackow, E. C. Effects of proinflammatory cytokines and bacterial toxins on neutrophil rheologic properties. *Crit. Care Med.* **26**, 1677–1682 (1998).
31. Bennett, R. E. et al. Tau induces blood vessel abnormalities and angiogenesis-related gene expression in P301L transgenic mice and human Alzheimer's disease. *Proc. Natl Acad. Sci. USA* **115**, E1289–E1298 (2018).
32. Haft-Javaherian, M. et al. Deep convolutional neural networks for segmenting 3D in vivo multiphoton images of vasculature in Alzheimer disease mouse models. Preprint at *arXiv* https://arxiv.org/abs/1801.00880 (2018).
33. Villringer, A. et al. Imaging of leukocytes within the rat brain cortex in vivo. *Microvasc. Res.* **42**, 305–315 (1991).
34. Ishikawa, M. et al. Leukocyte plugging and cortical capillary flow after subarachnoid hemorrhage. *Acta Neurochir.* **158**, 1057–1067 (2016).
35. Kloner, R. A. No-reflow phenomenon: maintaining vascular integrity. *J. Cardiovasc. Pharmacol. Ther.* **16**, 244–250 (2011).
36. Engler, R. L., Schmid-Schönbein, G. W. & Pavelec, R. S. Leukocyte capillary plugging in myocardial ischemia and reperfusion in the dog. *Am. J. Pathol.* **111**, 98–111 (1983).
37. Chibber, R., Ben-Mahmud, B. M., Chibber, S. & Kohner, E. M. Leukocytes in diabetic retinopathy. *Curr. Diabetes. Rev.* **3**, 3–14 (2007).
38. Santisakultarm, T. P. et al. Stalled cerebral capillary blood flow in mouse models of essential thrombocythemia and polycythemia vera revealed by in vivo two-photon imaging. *J. Thromb. Haemost.* **12**, 2120–2130 (2014).
39. Ilesanmi, O. O. Pathological basis of symptoms and crises in sickle cell disorder: implications for counseling and psychotherapy. *Hematol. Rep.* **2**, e2 (2010).
40. Zuliani, G. et al. Markers of endothelial dysfunction in older subjects with late onset Alzheimer's disease or vascular dementia. *J. Neurol. Sci.* **272**, 164–170 (2008).
41. Iadecola, C. Vascular and metabolic factors in Alzheimer's disease and related dementias: introduction. *Cell. Mol. Neurobiol.* **36**, 151–154 (2016).
42. Zenaro, E. et al. Neutrophils promote Alzheimer's disease-like pathology and cognitive decline via LFA-1 integrin. *Nat. Med.* **21**, 880–886 (2015).
43. Goldsmith, H. S. Alzheimer's disease can be treated: why the delay? *Surg. Neurol. Int.* **8**, 133 (2017).
44. Blinder, P. et al. The cortical angiome: an interconnected vascular network with noncolumnar patterns of blood flow. *Nat. Neurosci.* **16**, 889–897 (2013).

Acknowledgements

This work was supported by the National Institutes of Health grants Nos. AG049952 (C.B.S.), NS37853 (C.I.), NS097805 (L.P.) and AG031620 (N.N.), the Alzheimer's Drug Discovery Foundation (C.B.S.), the Alzheimer's Art Quilt Initiative (C.B.S.), the BrightFocus Foundation (C.B.S.), European Research Council grant No. 615102 (S.L.), the DFG German Research Foundation (O.B.), a National Science Foundation Graduate Research Fellowship (J.C.H.), the L'Oréal Fellowship for Women in Science (N.N.) and used computing resources at CALMIP (S.L.). We thank F. Lauwers for the human vascular data, P. Tsai, P. Blinder and D. Kleinfeld for the mouse vascular data and M. Gulinello for guidance on behavior experiments. Finally, we thank J.R. Fetcho, J.H. Goldberg and M.I. Kotlikoff for commenting on the manuscript.

Author contributions

J.C.C.H., O.B., S.L., N.N. and C.B.S. conceived the study. J.C.C.H., O.B. and C.J.K. performed the in vivo imaging experiments. MH., G.O. and Y.K. developed custom software for data analysis. M.H. developed custom machine learning algorithms for image segmentation. O.B. conducted the behavioral studies. L.P. and C.I. conducted the ALS-MRI experiments. D.R. conducted laser speckle imaging studies. M.B., M.P., V.D., A.S., Y.D. and S.L. performed the blood flow simulations. M.C.C. and S.S. did the stall analyses in the TgCNRD8 mouse model. J.C.C.H, O.B., C.J.K., V M., L.K.V., I.I., Y.K., J.Z., J.D.B. and E.D. contributed to the analysis of in vivo imaging experiments. J.C.C.H., O.B., N.N. and C.B.S. wrote the paper with contributions from M.H., M.C.C., L.P., C.L., C.I. and S.L. All authors edited and commented on the manuscript.

Competing interests

The authors declare no competing interests.

Additional information

Supplementary information is available for this paper at https://doi.org/10.1038/s41593-018-0329-4.

Methods

Animals and surgical preparation. All animal procedures were approved by the Cornell Institutional Animal Care and Use Committee (protocol Nos. 2009–0043 and 2015–0029) and were performed under the guidance of the Cornell Center for Animal Resources and Education. We used adult transgenic mice as mouse models of Alzheimer's disease, including the APP/PS1 line (B6.Cg-Tg (APPswe, PSEN1dE9) 85Dbo/J; MMRRC_034832-JAX, The Jackson Laboratory)[45] and the 5xFAD line (B6SJL-Tg(APPSwFlLon, PSEN1 *M146L*L286V)6799Vas/Mmjax; MMRRC Stock No: 34840-JAX, The Jackson Laboratory)[46]. Littermate WT mice (C57BL/6) were used as controls. Animals were of both sexes and ranged in age from 12 to 100 weeks.

For cranial window implantation, mice were anesthetized under 3% isoflurane on a custom-built stereotactic surgery frame and then maintained on ~1.5% isoflurane in 100% oxygen. Once unresponsive to a toe pinch, mice were given 0.05 mg per 100 g mouse weight of glycopyrrolate (Baxter, Inc.) or 0.005 mg per 100 g of atropine (54925-063-10, Med-Pharmex, Inc.) to prevent lung secretions; 0.025 mg per 100 g of dexamethasone (07-808-8194, Phoenix Pharm, Inc.) to reduce post-surgical inflammation; and 0.5 mg per 100 g of ketoprofen (Zoetis, Inc.) to reduce post-surgical inflammation and provide post-surgical analgesia. Glycopyrrolate and ketoprofen were injected intramuscularly, while atropine and dexamethasone were injected subcutaneously. Bupivacaine (0.1 ml, 0.125%;Hospira, Inc.) was subcutaneously administered at the incision site to provide a local nerve block. Animals were provided with 1 ml per 100 g mouse weight of 5% (w/v) glucose in normal saline subcutaneously every hour during the procedure. We used a thermometer and feedback-controlled heating blanket (40-90-8D DC, FHC) to maintain body temperature at 37 °C. The head was shaved and washed three times with alternating 70% (v/v) ethanol and iodine solution (AgriLabs). A 6 mm-diameter craniotomy was performed over the cerebral cortex using a high-speed drill (HP4-917-21, Fordom) using bits of diameter 1.4, 0.9, 0.7 and 0.5 mm (Fine Science Tools) for different steps in the craniotomy procedure. The craniotomy was then covered with a sterile 8 mm-diameter glass coverslip (11986309, Thermo Scientific) and glued onto the remaining skull with cyanoacrylate adhesive (Loctite) and dental cement (Co-Oral-Ite Dental). All procedures were performed using sterile technique.

Once the craniotomy was completed, mice were returned to their cages and given injections of 0.025 mg per 100 g of dexamethasone and 0.5 mg per 100 g of ketoprofen subcutaneously 1 and 2 days after surgery, and all cages were placed over a heating pad during this period. Animals were given at least 2 weeks to recover from cranial window implantation before experimentation, to minimize inflammation from the surgical procedure. Animals were excluded from further study if the clarity of the imaging window was insufficient for 2PEF imaging.

In vivo two-photon microscopy. During imaging sessions, mice were anesthetized with 3% isoflurane, placed on a custom stereotactic frame and administered glycopyrrolate or atropine and glucose as described above. During imaging, anesthesia was maintained with ~1.5% isoflurane in 100% oxygen, with small adjustments made to the isoflurane to maintain the respiratory rate at ~1 Hz. They were kept at 37 °C with a feedback-controlled heating pad.

To fluorescently label the microvasculature, Texas Red dextran (40 µl, 2.5%, molecular weight (MW) = 70,000 kDA, Thermo Fisher Scientific) in saline was injected retro-orbitally immediately before imaging. In some animals, Aβ deposits were labeled using methoxy-X04[47]. In early experiments using methoxy-X04 obtained directly from Professor Klunk at the University of P ttsburgh, we retro-orbitally injected 40 µl of 1 mg ml^{-1} methoxy-X04 in 0.9% saline (adjusted to pH 12.0 with 0.1 N NaOH) immediately before imaging. In later experiments using methoxy-X04 available commercially from Tocris, we intraperitoneally injected methoxy-X04 (dissolved in DMSO at 100 mM) 1 day before imaging at a dose of 1 mg 100 g^{-1}. We observed no obvious differences in amyloid labeling between these two administration approaches. In some animals, leukocytes and blood platelets were labeled with a retro-orbital injection of Rhodamine 6 G (0.1 ml, 1 mg ml^{-1} in 0.9% saline, Acros Organics, Pure)[38]. Leukocytes were distinguished from blood platelets with a retro-orbital injection of Hoechst 33342 (50 µl, 4.8 mg ml^{-1} in 0.9% saline, Thermo Fisher Scientific). Texas Red (and methoxy-X04, when given retro-orbitally) was dosed in a single syringe, while Rhodamine 6 G and Hoechst were dosed together in a second syringe.

Three-dimensional images of the cortical vasculature and measurement of red blood cell flow velocity in specific vessels were obtained using a custom-built 2PEF microscope. Imaging was done using 830 nm, 75 fs pulses from a Ti:Sapphire laser oscillator (MIRA HP pumped by a Verdi-V18 or Vision S, Coherent) and 900 nm, 75 fs pulses from a second Ti:Sapphire laser oscillator (Vision S, Coherent). Lasers were scanned by galvonometric scanners (1 frame s^{-1}) and focused into the sample using a 20× water-immersion objective lens for high-resolution imaging (numerical aperture of 1.0, Carl Zeiss Microscopy; or numerical aperture of 0.95, Olympus), or a 4× objective for mapping of the cortical surface vasculature (numerical aperture of 0.28, Olympus). The emitted fluorescence was detected on either a two-channel detection system or, for later datasets, an upgraded four-channel detection system. On the two-channel system, the fluorescence was split by a 600 nm-long-pass dichroic and two successive image stacks were acquired first with 645/45 nm (center wavelength/bandwidth) and 575/25 nm bandpass filters to image Texas Red and Rhodamine 6 G, respectively, and then with 645/65 nm and 460/50 nm filters to image Texas Red and both methoxy-X04 and Hoescht (on the same channel), all under 830 nm excitation. On the four-channel system, a secondary long-pass dichroic at 520 nm was followed by tertiary long-pass dichroics at 458 nm and one at either 562 or 605 nm. Emission was detected on four photomultiplier tubes through the following emission filters: 417/60 nm for Hoechst, 494/41 nm for methoxy-X04, 550/49 nm for Rhodamine 6 G and 641/75 nm for Texas Red. Laser excitation was 830 nm except when trying to image deep cortical tissue in animals where only Texas Red was present, in which case 900 nm excitation was used. Laser scanning and data acquisition were controlled by ScanImage software[48]. To visualize the cortical vasculature, stacks of images spaced at 1 µm axially were taken to a cortical depth of 300–500 µm.

For imaging of neutrophils labeled with anti-Ly6G antibodies labeled with Alexa488, imaging was performed on a custom-built 2PEF microscope at the Wellman Center for Photomedicine. In these animals, neutrophils were labeled with a tail vein injection of anti-Ly6G-Alexa488 (0.1 mg kg^{-1} animal weight, 127626-Biolegend) at the same time as the labeling of blood plasma with Texas Red dextran. Imaging was done using 750 nm, 80 fs pulses from a Ti:Sapphire laser oscillator (Spectra-Physics Mai Tai). The laser beam was scanned by polygon scanners (30 frames s^{-1}) and focused into the sample using a 40× water-immersion objective lens for high-resolution imaging (numerical aperture of 0.80, Olympus), or a 10× objective for mapping of the cortical surface vasculature (numerical aperture of 0.30, Olympus). The emitted fluorescence was detected on photomultiplier tubes through the following emission filters: 525/50 nm for Alexa488 and 605/50 nm for Texas Red. Laser scanning and data acquis tion were controlled by custom-built software. Stacks of images spaced at 1 µm axially were taken to a cortical depth of 100–200 µm.

Quantification of capillary network topology and capillary segment stalling. The 2PEF images of vascular networks were manually traced in three dimensions to create a vectorized skeleton that represents the cortical vasculature using custom-written tracing software. The researchers producing these tracings were blinded to the genotype of the animal and any treatment it had received. Volumes of these image stacks where vessels could not be readily identified and traced were excluded from all analysis. These regions were typically deep and near the edges of the imaged volume, or occasionally directly underneath a large surface vessel. Vessel segments were classified as surface and penetrating arterioles and capillaries, or as ascending and surface venules. All vessels less than 10 µm in diameter were classed as capillaries. Large-surface arterioles were distinguished from large-surface venules based on morphology (arterioles were of smaller diameter, had smoother walls and less tortuosity and tended to branch more symmetrically and in Y-shaped junctions compared to venules). Other arterioles or venules were classed by tracing their connectivity to readily identifiable large vessels.

Each capillary segment in these images was then manually classed as either flowing or stalled based on the motion of RBCs during the entire time each capillary was visible in the three-dimensional image stack. Texas Red dextran labels blood plasma but not blood cells, so RBCs and other blood cells are shown as dark patches in the vessel lumen. The motion of these dark patches indicates flowing blood cells. Each capillary segment was visible in a minimum of around five successive frames in the three-dimensional image stack, or for ~5 s (capillaries not oriented parallel to the cortical surface were observed for markedly more frames). We scored a capillary segment as stalled if we did not see motion of the RBCs and other cells in the capillary segment over this observation time. This manual scoring of capillaries, as either flowing or stalled, was performed with the researcher blinded to the genotype and treatment status of the animal. In addition, scoring was performed using only the image data visible on the Texas Red imaging channel. All animals included in our analysis had at least 800 capillary segments scored as flowing or stalled. Animals with fewer characterized capillaries were excluded.

Using the traced vascular network, the topologically shortest path from each flowing or stalled capillary to the nearest penetrating arteriole and ascending venule was calculated using Dijkstra's algorithm[49].

Distinguishing causes of capillary stall. In some animals, once capillary stalls were identified we used the additional fluorescent labels to determine what was blocking blood flow in the capillary segment. Stalled capillary segments with a cell-shaped object labeled with both Rhodamine 6 G and Hoechst present were scored as having a leukocyte present; stalled segments with punctate objects labeled with Rhodamine 6 G alone were scored as having platelet aggregates; stalled capillary segments with only RBCs present were classed as RBC stalls. We determined what fraction of stalled capillaries had only a leukocyte, a leukocyte with one or more RBCs present, only platelet aggregates, platelet aggregates with RBCs, and only RBCs. With this labeling scheme, we were unable reliably to distinguish platelet aggregates when a leukocyte was present. Additional experiments used a low dose of Alexa488-labeled anti-Ly6G antibodies to assess the type of leukocyte associated with capillary stall.

We assessed whether the diameter of flowing and stalled capillaries was different, on average. First, image stacks were linearly interpolated to have an isotropic 1 µm voxel size. To reduce salt-and-pepper noise in the vascular

images, we filtered using a three-dimensional 5×5×5 pixel Gaussian filter. We then corrected for unevenness in the image intensity by filtering the image (85×85 pixel-sized mean filter) and subtracted this from the Gaussian filtered image. The resulting image was binarized using Otsu's method[50]. Finally, objects smaller than 1,000 voxels were eliminated, where voxels were considered part of the same connected object whenever they shared at least one corner. We then used this binarized image to correct the manual tracing of the vasculature by shifting the centerline so that it was equidistant from the vessel boundaries (done within a 10 µm neighborhood to avoid confusion between neighboring capillaries). Every 5 µm along the centerline of each capillary segment, we estimated the vessel radius by finding the shortest distance from the centerline to the vessel boundary. Measurements <2 µm or >10 µm were excluded, as these probably reflected imaging artifacts, and we averaged across all measurements for each capillary segment.

Administration of antibodies against Ly6G or LFA-1 to interfere with capillary stalling. We treated APP/PS1 and 5xFAD mice with intraperitoneal injections of monoclonal antibodies against lymphocyte antigen 6 complex, locus G (Ly6G) (α-Ly6G, clone 1A8, 4 mg kg^{-1}, BD Biosciences) or an isotype control antibody (Rat IgG2a, κ, 4 mg kg^{-1}, BD Biosciences). In addition, APP/PS1 mice were treated with retro-orbital or intraperitoneal injections of monoclonal antibodies against lymphocyte functional antigen 1 (α-LFA-1; M17/4 clone, BD Biosciences; 4 mg kg^{-1}). The same cortical capillary bed was imaged in anesthetized mice immediately before and at 60–90 min after treatment. Mice were randomly assigned to receive treatment or isotype control antibodies, and the experimenter was blinded to both mouse genotype and whether the antibody was the treatment or control during the experiment. Quantification of stalled capillaries was performed by researchers blinded to imaging time, animal genotype and treatment type.

Behavior experiments. All experiments were performed under red lighting in an isolated room. The position of the mouse's nose was automatically traced by Viewer III software (Biobserve). In add tion to the automatic results obtained by Viewer III software, a blinded experimenter independently scored mouse behavior manually. Animals were taken into the behavior room 1 h before the experiment. Behavioral analysis was conducted at baseline and at 3 and 24 h after injection with α-Ly6G, α-LFA-1 or isotype control antibodies (IP 4 mg kg^{-1}). The α-Ly6G-treated APP/PS1 mice were then treated every 3 days for 4 weeks (2 mg kg^{-1}intraperitoneally) and behavior experiments were repeated. The object replacement, Y-maze, balance beam walk and forced swim tests were performed at all time points. The NOR task was performed only at baseline and the 4-week time point, to avoid animals becoming accustomed to the objects. For experiments with APP/PS1 mice and α-Ly6G, animals were ~11 months of age at the start of the experiment. For experiments with APP/PS1 mice and α-LFA-1, animals were 11–13 months of age. For experiments with 5xFAD mice and α-Ly6G, animals were 5–6 months of age. Mice were randomly assigned to receive treatment or isotype control antibodies, and the experimenter was blinded to both mouse genotype and whether the antibody was the treatment or control during the experiment.

Object replacement test. The object replacement task evaluated spatial memory performance. All objects used were first validated in a separate cohort of mice to ensure that no intrinsic preference or aversion was observed, and animals explored all objects similarly. Exploration time for the objects was defined as any time when there was physical contact w th an object (whisking, sniffing, rearing on or touching it) or when the animal was oriented toward the object and the head was within 2 cm of it. In trial 1, mice were allowed to explore two identical objects for 10 min in the arena and then returned to their home cage for 60 min. Mice were then returned to the testing arena for 3 min with one object moved to a novel location (trial 2). Care was taken to ensure that the change of placement altered both the intrinsic relationship between objects (for example, rotation of the moved object) and the position relative to internal visual cues (for example, new location in the arena; one wall of testing arena had a pattern). At subsequent time points, new object positions and new pairs of objects (from the validated pool of objects) were used to maintain animal interest. In addition to using the tracking software to determine the object exploration times, the time spent at each object was manually scored by an independent experimenter who was blinded to the genotype and treatment. The preference score (%) for object replacement tasks was calculated, from the data in trial 2, as ([exploration time of the novel object]/[exploration time of both objects])×100. Automated tracking and manual scoring yielded similar results across groups, so we report the automated tracking results.

Y-maze. The Y-maze task was used to measure working memory, by quantifying spontaneous alternation between arms of the maze. The Y-maze consisted of three arms at 120° and was made of light gray plastic. Each arm was 6 cm wide and 36 cm long, and had walls 12.5 cm in height. The maze was cleaned with 70% ethanol after each mouse. A mouse was placed in the Y-maze and allowed to explore for 6 min. Behavior was monitored, recorded and analyzed using the Viewer software. A mouse was considered to have entered an arm if the whole body (except for the tail) entered it, and to have exited if the whole body (except for the tail) exited the arm. If an animal consecutively entered three different arms, that was counted as an alternating trial. Because the maximum number of triads is the total number of arm entries minus 2, the spontaneous alternation score was calculated as ([number of alternating triads]/([total number of arm entries] − 2)).

Novel object recognition test. The NOR task measures recognition memory and is based on rodents' innate preference for exploring novel objects. This test was conducted only at baseline and after 4 weeks of treatment. The testing approach was identical to the object replacement task, but with a novel object placed at the location of one of the initial objects in trial 2. To exclude preference bias for particular objects in the first trial, one animal would see two of object A and another animal two of object B. In the second trial, to test for preference for a novel object, both animals saw one of object A and one of object B. For the repeat of the test at 4 weeks, we used new objects C and D.

ELISA assay. After the conclusion of the behavior experiments, the APP/PS1 animals that had received α-Ly6G or isotype control antibodies every 3 days for a month were killed by lethal injection of pentobarbital (5 mg per 100 g). Brains were quickly extracted and divided along the centerline. One half was immersed in 4% paraformaldehyde in phosphate buffered saline (PBS) for later histological analysis and the other half was snap-frozen in liquid nitrogen.

The frozen APP/PS1 mouse hemi-brains (Iso-Ctr: $n=6$, 11.5–12.5 months old; α-Ly6G: $n=7$, 11.5–12.5 months old) were weighed and homogenized in 1 ml PBS containing complete protease inhibitor (Roche Applied Science) and 1 mM AEBSF (Sigma) using a Dounce homogenizer. The homogenates were then sonicated and centrifuged at 14,000 *g* for 30 min at 4 °C. The supernatant (PBS-soluble fraction) was removed and stored at −80 °C. The pellet was re-dissolved in 0.5 ml 70% formic acid, sonicated and centrifuged at 14,000 *g* for 30 min at 4 °C, and the supernatant was removed and neutralized using 1 M Tris buffer at pH 11.0. Protein concentration was measured in the PBS-soluble and formic acid-soluble fractions using the Pierce BCA Protein Assay (Thermo Fischer Scientific). The PBS-soluble fraction extracts were diluted 1:5; formic acid extracts were diluted 1:1 after neutralization. These brain extracts were analyzed by sandwich ELISA for $A\beta_{1-40}$, $A\beta_{1-42}$ and Aβ aggregates using commercial ELISA kits and following the manufacturer's protocol ($A\beta_{1-40}$: KHB3481; $A\beta_{1-4}2$: KHB3441; Aβ aggregates: KHB3491, Thermo Fisher Scientific). The Aβ concentration was calculated by comparing sample absorbance with that of known concentrations of synthetic $A\beta_{1-40}$ and $A\beta^{1-42}$ standards on the same plate. Data were acquired with a Synergy HT plate reader (Biotek) and analyzed using Gen5 software (BioTek) and Prism (Graphpad).

Statistical analysis. Boxplots were created using Prism7 (GraphPad). The box extends between the values for the 25th and 75th percentiles of the data. The whiskers extend 1.5 times the difference between the values of the 75th and 25th percentiles of the data from the top and bottom of the box. Values lying outside the whiskers were defined as outliers, and the mean was computed excluding these outliers. The median is indicated with a black horizontal line inside the box, while the mean is indicated with a red horizontal line. Violin plots were created using the statistical software package R.

Data in all groups were tested for normality using the D'Agostino–Pearson omnibus normality test. Parametric statistics were used only if the data in all groups in the comparison were normally distributed. The statistical significance of differences between multiple groups was determined using one-way ANOVA followed by Tukey's multiple comparison correction for normally distributed data, and using one-way Kruskal–Wallis ANOVA followed by Dunn's multiple comparison correction for data with non-normal distribution. To compare baseline and post-treatment measurements at multiple time points with non-normal data, Friedman one-way repeated measures non-parametric ANOVA followed by Dunn's multiple comparison correction was used. Statistical comparisons between two groups were performed using Student's *t*-test or paired *t*-test for normally distributed data, or with the Mann–Whitney test or Wilcoxon matched-pairs test for data with non-normal distribution. $P<0.05$ was considered statistically significant. All statistical analysis was performed using Prism7 (GraphPad).

We use a standardized set of significance indicators across all figures in this manuscript. For comparisons between groups: $^{*}P<0.05$, $^{**}P<0.01$, $^{***}P<0.001$, $^{****}P<0.0001$. For matched comparisons before and after treatment: $^{+}P<0.05$, $^{++}P<0.01$. Details of the groups compared, animal and capillary numbers, sex distributions statistical tests, exact *P* values and explanatory notes for individual panels are included in the figure captions.

Additional methodological details. Additional information on the methods used in this study is available in the Supplementary Methods.

Reporting Summary. Further information on research design is available in the Nature Research Reporting Summary linked to this article.

Code availability

Code for 3D tracing, vessel segmentation, analysis of linescan data and determination of amyloid density around capillaries can be obtained by contacting

N.N. or C.B.S. Code for simulation of blood flow in vascular networks can be obtained by contacting S.L.

Data availability

The raw data reported in this manuscript are archived at https://doi.org/10.7298/9PR3-D773.

References

45. Jankowsky, J. L. et al. Mutant presenilins specifically elevate the levels of the 42 residue beta-amyloid peptide in vivo: evidence for augmentation of a 42-specific gamma secretase. *Hum. Mol. Genet.* **13**, 159–170 (2004).
46. Oakley, H. et al. Intraneuronal beta-amyloid aggregates, neurodegeneration, and neuron loss in transgenic mice with five familial Alzheimer's disease mutations: potential factors in amyloid plaque formation. *J. Neurosci.* **26**, 10129–10140 (2006).
47. Klunk, W. E. et al. Imaging Abeta plaques in living transgenic mice with multiphoton microscopy and methoxy-X04, a systemically administered Congo red derivative. *J. Neuropathol. Exp. Neurol.* **61**, 797–805 (2002).
48. Pologruto, T. A., Sabatini, B. L. & Svoboda, K. ScanImage: flexible software for operating laser scanning microscopes. *Biomed. Eng. Online* **2**, 13 (2003).
49. Dijkstra, E. W. A note on two problems in connexion with graphs. *Numer. Math.* **1**, 269–271 (1959).
50. Otsu, N. A threshold selection method from gray-level histogram. *IEEE Trans. Syst. Man. Cybern.* **9**, 62–66 (1979).

Reporting Summary

Statistical parameters

When statistical analyses are reported, confirm that the following items are present in the relevant location (e.g. figure legend, table legend, main text, or Methods section).

n/a	Confirmed	
☐	☒	The exact sample size (*n*) for each experimental group/condition, given as a discrete number and unit of measurement
☐	☒	An indication of whether measurements were taken from distinct samples or whether the same sample was measured repeatedly
☐	☒	The statistical test(s) used AND whether they are one or two sided *Only common tests should be described solely by name; describe more complex techniques in the Methods section.*
☒	☐	A description of all covariates tested
☐	☒	A description of any assumptions or corrections, such as tests of normality and adjustment for multiple comparisons
☐	☒	A full description of the statistics including central tendency (e.g. means) or other basic estimates (e.g. regression coefficient) AND variation (e.g. standard deviation) or associated estimates of uncertainty (e.g. confidence intervals)
☒	☐	For null hypothesis testing, the test statistic (e.g. *F*, *t*, *r*) with confidence intervals, effect sizes, degrees of freedom and *P* value noted *Give P values as exact values whenever suitable.*
☒	☐	For Bayesian analysis, information on the choice of priors and Markov chain Monte Carlo settings
☒	☐	For hierarchical and complex designs, identification of the appropriate level for tests and full reporting of outcomes
☐	☒	Estimates of effect sizes (e.g. Cohen's *d*, Pearson's *r*), indicating how they were calculated
☐	☒	Clearly defined error bars *State explicitly what error bars represent (e.g. SD, SE, CI)*

Software and code

Policy information about availability of computer code

Data collection	All in vivo mouse data was taken with a custom built 2 photon microscope, Biospec 70/30, Bruker and custom built laser speckle setup. Histology sections have been analyzed by a Zeiss Examiner.D1 AXIO, behavioral data was collected using ViewerIII from BIOBSERVE (Germany), scanimage (Vidrio Tech.), and flow cytometry data was taken on a Guava easyCyte Flow Cytometer (EMD Millipore Corporation).
Data analysis	Data has been analyzed using MATLAB (The MathWorks, Inc), ImageJ (NIH), FlowJo (LLC), Gen5 (BioTeck), Imaris 8 (Bitplane), R 3.5.1 (The R Foundation), G*Power, and Prism7 (GraphPad).

Data

Policy information about availability of data

All manuscripts must include a data availability statement. This statement should provide the following information, where applicable:

- Accession codes, unique identifiers, or web links for publicly available datasets
- A list of figures that have associated raw data
- A description of any restrictions on data availability

The data reported in this manuscript are archived at https://doi.org/10.7298/9PR3 D773.

Field-specific reporting

Please select the best fit for your research. If you are not sure, read the appropriate sections before making your selection.

☒ Life sciences ☐ Behavioural & social sciences ☐ Ecological, evolutionary & environmental sciences

Life sciences study design

All studies must disclose on these points even when the disclosure is negative.

Sample size	In most cases, sample sizes for comparisons across groups were determined from power analysis calculations. The data on capillary stall incidence in Fig. 1c and d in APP/PS1 vs. wt mice is significantly overpowered, as this data includes experiments that yielded the initial discovery of elevated capillary stalling in APP/PS1 mice as well as all subsequent baseline data. For measurements of the cellular cause of capillary stalls (Fig. 2a and b), we anticipated finding ~20 stalls per mouse (~2% of 1,000 characterized capillaries). Assuming each possible stall cause was equally likely and wanting to resolve these percentages to +/ 10% at a 95% confidence interval, then binomial statistics implied the need for ~100 capillary stalls, or about five mice. For 2PEF measurements of penetrating arteriole blood flow (Fig. 3b and c), ASL MRI measurements of cortical perfusion (Fig. 3d and e), and behavioral experiments (Fig. 4) comparing APP/PS1 and wt mice before and after antibody treatment, we used a matched pairs study design, estimates of measurement variability from published and preliminary data, and estimates of minimal biologically relevant effect size to determine minimum group sizes using G*Power. This yielded minimum group sizes of 5 mice for 2PEF measurements of penetrating arteriole blood flow and 10 mice for ASL MRI and behavioral experiments. In subsequent experiments with other mouse models and other treatments we continued using these group sizes.
Data exclusions	Animals were excluded from further study if the clarity of the imaging window was insufficient for 2PEF imaging. All animals included in our analysis of the frequency of capillary stalling had at least 800 capillary segments scored as flowing or stalled. Animals with fewer characterized capillaries were excluded.
Replication	Experiments to determine the fraction of capillaries stalled and the cell type responsible for stalls have been conducted by several different experimenters across different microscopes, and even different laboratories. The manual scoring of capillaries as flowing or stalled was performed with the researcher blinded to the genotype and treatment status of the animal. Blood flow experiments (line scans, ALS MRI, and Laser Speckle Imaging) were conducted and analyzed with the experimenter blinded to the treatment and genotype of the animals. Behavior experiments in APP/PS1 mice were done twice with two independent groups with similar results. The experimenter was blinded to the treatment and animal genotype. In addition to the automatic results we obtained, a blinded experimenter independently scored mouse behavior manually. All manual and automated analysis results concurred.
Randomization	Animals were matched by age and similar numbers of male and female animals were used in nearly all comparisons. Controls were litter mates. Mice were randomly selected for treatment or control groups. All treatments were given by a different researcher where possible to ensure blinding.
Blinding	During experiments comparing the impact of treatments, the experimenter was blinded to the treatment and genotype of the mouse. All analysis was conducted with the experimenter blinded to the genotype, treatment, and time point of the data. Image processing was done also blinded to genotype and treatment, if possible (note that AD mouse models can be readily distinguished at some ages by presence of amyloid plaques).

Reporting for specific materials, systems and methods

Materials & experimental systems		Methods	
n/a	Involved in the study	n/a	Involved in the study
☒	☐ Unique biological materials	☒	☐ ChIP seq
☐	☒ Antibodies	☐	☒ Flow cytometry
☒	☐ Eukaryotic cell lines	☐	☒ MRI based neuroimaging
☒	☐ Palaeontology		
☐	☒ Animals and other organisms		
☒	☐ Human research participants		

Antibodies

Antibodies used

Antibodies:
Antibodies were validated in preliminary experiments involving serial dilutions (Ly6G). The final concentration used for each antibody is:
Ly6G (for in vivo imaging): clone 1A8, Alexa 488 labeled, Catalog No.560257, BD Biosciences
Ly6G (for in vivo blocking of adherence):clone 1A8, FITC labeled, Catalog No.551460, BD Biosciences
LFA 1: clone M17/4, CD11b, Catalog No. 550528 BD Biosciences
Iso Ctr: clone IgG2a, k, Catalog No. 553387, BD Biosciences

in vivo imaging:
Ly6G antibodies (0.1 mg/kg), i.v. injection

Blocking adherence or causing depletion:
acute experiments: Ly6G or isotype control antibodies (4 mg/kg), i.p. injection
chronic experiments: Ly6G or isotype control antibodies (2 mg/kg), i.p. injection
LFA 1 experiments: LFA 1 or saline control injection (4 mg/kg), retro orbital injection (blood flow expts.) or i.p. injection (behavioral expts.)

Flow cytometry:
Chronic experiments: 24h after Ly6G or control injection (4 mg/kg), i.p. injection
Neutrophil determination: anti CD45 (Catalog No.5560695, BD Bioscience), anti CD11b (Catalog No.561690, BD Bioscience) and anti Ly6G (551460, BD Bioscience).

Histology:
Chronic treatment experiment: Sections have been incubated with 1% Thioflavin S (T1892, Sigma) for 10 min at room temperature and washed twice with 80% ethanol for 2 min and counter stained with and 1:5000 DAPI (Sigma)

Validation

Ly6G (for in vivo imaging) has been validated for example in: Journal of Experimental Medicine Apr 2012, 209 (4) 819 835; DOI: 10.1084/jem.20112322
Ly6G (for in vivo blocking of adherence):clone 1A8, FITC labeled, BD Biosciences, has been used widely for flow cytometry and in vivo imaging: Journal of Immunology Research, 2018, (1), (2018)
LFA 1: clone M17/4 has been used for in vivo studies and behavioral studies for example in Nature Medicine volume 21, pages 880 886 (2015)
CD45 widely used and validated references on the BD Biosciences web page
CD11b widely used and validated references on the BD Biosciences web page
Iso Ctr: clone IgG2a, k, BD Biosciences targets an unknown sequence

Animals and other organisms

Policy information about studies involving animals; ARRIVE guidelines recommended for reporting animal research

Laboratory animals

Heterozygous APP/PS1 mice have been used in this study (The Jackson Laboratory (Bar Harbor, ME)). These mice over express the amyloid precurser protein (APP) (Mo/HuAPP695swe) together with the human muted presenilin 1 (PS1 dE9) gene driven under the prion (PrP) promoter.
As a second mouse model we used TgCRND8 that over expresses the APP gene 695 (KM670/671NL+V717F) under the PrP promoter.
As a third mouse model we used 5xFAD mice (The Jackson Laboratory) that overexpress APP with the following mutations (Swedish (K670N, M671L), Florida (I716V), and London (V717I)) along with mutated PS1 with the following mutations (M146L and L286V), under the Thy1 promoter.
12 90 weeks old male and female (APP/PS1 n=28 and wild type n=12) mice have been used for the analyses done in figure 1.
Antibody injected animals to determine blood flow and number of stalls after Ly6G treatment have been male and female APP/PS1 mice 3 4 month: APP/PS1, α Ly6G n=5; APP/PS1 Iso Ctl, n=5;and wt α Ly6G, n=5; 11 14 month: APP/PS1, α Ly6G n=3; and APP/PS1 Iso Ctl, n=3)
ALS MRI has been performed with 7 9 month old male and female APP/PS1 mice (APP/PS1, α Ly6G n=10; APP/PS1 Iso Ctl, n=10; and wt α Ly6G, n=10)
Capillary stalls and flow in 5xFAD mice: 5 7 months of age, wt α Ly6G: 3 mice; 5xFAD Iso Ctr: 3 mice,; and 5xFAD α Ly6G: 3 mice.
Behavior experiments used 11 month old APP/PS1 male and female animals have been used (APP/PS1, α Ly6G n=11; APP/PS1 Iso Ctl, n=9; wt α Ly6G, n=10; and wt Iso Ctl, n=10). Brains for the ELISA and histology experiments has been from the the ones

	from behavioral experiments For behavior experiments animal of both sexes got randomly distributed into experimental group, APP/PS1 mice and α LFA 1, animals were 11 13 months of age (APP/PS1, α LFA 1 n=10; APP/PS1 Iso Ctl, n=10; wt α LFA 1, n=7; and wt Iso Ctl, n=8). For behavior experiments animal of both sexes got randomly distributed into experimental group, 5xFAD mice and α Ly6G, animals were 5 6 months of age (5xFAD, α Ly6G n=8; 5xFAD Iso Ctl, n=8; and wt α Ly6G, n=10).
Wild animals	We did not use wild animals.
Field collected samples	We had no field collected samples.

Flow Cytometry

Plots

Confirm that:

☒ The axis labels state the marker and fluorochrome used (e.g. CD4 FITC).

☒ The axis scales are clearly visible. Include numbers along axes only for bottom left plot of group (a 'group' is an analysis of identical markers).

☒ All plots are contour plots with outliers or pseudocolor plots.

☒ A numerical value for number of cells or percentage (with statistics) is provided.

Methodology

Sample preparation	Blood from APP/PS1 and wt mice was collected from the submandibular vein and mixed with 1x RBC lysis buffer (00 4300 54, ThermoFisher Scientific). After incubation at room temperature for 10 min, the sample was centrifuged at 500 g for 5 min and the supernatant was removed. The cell pellet was re suspended in 500 uL of Hank's balanced salt solution (HBSS) supplemented with 1% bovine serum albumin (BSA) and centrifuged again; this washing procedure was repeated 3 times. Following isolation, neutrophils were re suspended at a density of 107 cells per ml in HBSS supplemented with 1% BSA. The cell samples were labeled at room temperature for 45 min with the following anti mouse antibodies: anti CD45 (560695, BD Bioscience), anti CD11b (557686, BD Bioscience) and anti Ly6G (551460, BD Bioscience). After washing the samples with HBSS samples have been re suspended in FACS buffer (1% BSA and 2mM EDTA in PBS), the remaining leukocytes were analyzed by flow cytometry
Instrument	Guava easyCyte Flow Cytometer (EMD Millipore Corporation)
Software	Data were analyzed using FlowJo software (FlowJo LLC)
Cell population abundance	In a first step dead cells that have a higher side scatter and lower forward scatter than living cells were gated based on FSC versus SSC to analyze viable cells. Then CD45 was used to gate all Leukocytes and CD11b with Ly6G to determine the neutrophils population.
Gating strategy	Relevant example is shown in Extended Data Fig. 7a

☒ Tick this box to confirm that a figure exemplifying the gating strategy is provided in the Supplementary Information.

Magnetic resonance imaging

Experimental design

Design type	Arterial spin labeling and anatomical T2 imaging was used to measure blood flow and structure in APP/PS1 and wild type mice before and 3 6 hr after Ly6G antibody or isotype control antibody treatment.
Design specifications	2 mice per day were imaged. Baseline measurements required a 40 min scan time. After about 48 h antibodies were i.p. injected and 3 6 h later animals were imaged for another 40 min. Mice age ranged from 6 9 month.
Behavioral performance measures	n/a

Acquisition

Imaging type(s)	Arterial spin labeling and T2 anatomical imaging
Field strength	7.0 Tesla
Sequence & imaging parameters	ASL imaging was based on a FAIR RARE pulse sequence that labeled the inflowing blood by global inversion of the equilibrium magnetization. The inversion recovery data from the imaging slice are acquired after selective inversion of the slice and after inversion of both the slice and the surrounding tissue. The difference of the apparent R1 relaxation rate images then yields a measure of the CBF: Detail: Three averages of one axial slice were acquired with a field of view of 15 × 15 mm, spatial resolution of 0.23 × 0.23 × 2 mm3, echo time TE of 5.36 ms, effective TE of 26.84 ms, repeat time TR of 10 s, and a RARE factor of 36. T2 images:

	Turbo RARE anatomical images were acquired with the following parameters: 10 averages of 14 slices with the same field of view and orientation as the ASL images, resolution = 0.078 × 0.078 × 1 mm3, TE = 48 ms, TR = 2000 ms, and a RARE factor of 10
Area of acquisition	Anatomical localizer images were acquired to find the transversal slice at a location approximately corresponding to Bregma 0.94 mm

Diffusion MRI ☐ Used ☒ Not used

Preprocessing

Preprocessing software	For computation of rCBF, the Bruker ASL perfusion processing macro was used. It uses the model of Kober, et al., and includes steps to mask out the background and ventricles. The masked rCBF images were exported to Analyze format on the MRI console. Statistics has been finalized in PRISM. F. Kober et al., High resolution myocardial perfusion mapping in small animals in vivo by spin labeling gradient echo imaging. Magnetic resonance in medicine 51, 62 67 (2004).
Normalization	n/a
Normalization template	n/a
Noise and artifact removal	n/a
Volume censoring	*Define your software and/or method and criteria for volume censoring, and state the extent of such censoring.*

Statistical modeling & inference

Model type and settings	Our primary comparisons are between the baseline measurements for wild type and AD mouse models (t test, as data were normally distributed), and a paired comparision of wt or AD mice before and after antibody treatment (paired t test, data were normally distributed).
Effect(s) tested	Measured cerebral blood flow in the same mice before and after treatment. Secondary measure comparing blood flow in wt and AD mice.

Specify type of analysis: ☐ Whole brain ☒ ROI based ☐ Both

Anatomical location(s)	The masked CBF images were exported to Analyze format on the MRI console. We then used the anatomical image to create a mask that outlined the entire cortical region,excluding the sinus, and averaged the CBF measurement across this region for each animal at each imaging time point. Analysis of ASL MRI data was conducted blinded to animal genotype and treatment.
Statistic type for inference (See Eklund et al. 2016)	voxel wise
Correction	n/a

Models & analysis

n/a	Involved in the study
☒	☐ Functional and/or effective connectivity
☒	☐ Graph analysis
☒	☐ Multivariate modeling or predictive analysis